

REPORT DOCUMENTATION PAGE			Form Approved OMB NO. 0704-0188	
<p>The public reporting burden for this collection of information is estimated to average 1 hour per response, including the time for reviewing instructions, searching existing data sources, gathering and maintaining the data needed, and completing and reviewing the collection of information. Send comments regarding this burden estimate or any other aspect of this collection of information, including suggestions for reducing this burden, to Washington Headquarters Services, Directorate for Information Operations and Reports, 1215 Jefferson Davis Highway, Suite 1204, Arlington VA, 22202-4302. Respondents should be aware that notwithstanding any other provision of law, no person shall be subject to any penalty for failing to comply with a collection of information if it does not display a currently valid OMB control number.</p> <p>PLEASE DO NOT RETURN YOUR FORM TO THE ABOVE ADDRESS.</p>				
1. REPORT DATE (DD-MM-YYYY) 25-08-2015		2. REPORT TYPE Conference Proceeding		3. DATES COVERED (From - To) -
4. TITLE AND SUBTITLE Blade Sections in Streamwise Oscillations into Reverse Flow			5a. CONTRACT NUMBER W911NF-13-1-0244	
			5b. GRANT NUMBER	
			5c. PROGRAM ELEMENT NUMBER 611102	
6. AUTHORS Joachim Hodara, Marilyn Smith, Kenneth Granlund, Karen Mulleners, Michael Ol, Anya Jones			5d. PROJECT NUMBER	
			5e. TASK NUMBER	
			5f. WORK UNIT NUMBER	
7. PERFORMING ORGANIZATION NAMES AND ADDRESSES Georgia Tech Research Corporation 505 Tenth Street NW  Atlanta, GA 30332 -0420			8. PERFORMING ORGANIZATION REPORT NUMBER	
9. SPONSORING/MONITORING AGENCY NAME(S) AND ADDRESS (ES) U.S. Army Research Office P.O. Box 12211 Research Triangle Park, NC 27709-2211			10. SPONSOR/MONITOR'S ACRONYM(S) ARO	
			11. SPONSOR/MONITOR'S REPORT NUMBER(S) 61963-EG.1	
12. DISTRIBUTION AVAILABILITY STATEMENT Approved for public release; distribution is unlimited.				
13. SUPPLEMENTARY NOTES The views, opinions and/or findings contained in this report are those of the author(s) and should not be construed as an official Department of the Army position, policy or decision, unless so designated by other documentation.				
14. ABSTRACT A low-Reynolds number rectilinear analog of the retreating blade problem is considered by computationally and experimentally studying a NACA0012 blade in spanwise oscillation in a free stream. Three-dimensional hybrid RANS-LES simulations with spanwise periodic boundary conditions and experimental flow visualization support the description of experimental				
15. SUBJECT TERMS Reverse Flow, Oscillating Airfoils, Oscillating Freestream				
16. SECURITY CLASSIFICATION OF:			17. LIMITATION OF ABSTRACT	15. NUMBER OF PAGES
a. REPORT UU	b. ABSTRACT UU	c. THIS PAGE UU	UU	19a. NAME OF RESPONSIBLE PERSON Marilyn Smith
				19b. TELEPHONE NUMBER 404-894-3065

## **Report Title**

Blade Sections in Streamwise Oscillations into Reverse Flow

### **ABSTRACT**

A low-Reynolds number rectilinear analog of the retreating blade problem is considered by computationally and experimentally studying a NACA0012 blade in spanwise oscillation in a free stream. Three-dimensional hybrid RANS-LES simulations with spanwise periodic boundary conditions and experimental flow visualization support the description of experimental direct force measurements for a wide range reduced frequencies and advance ratios, including fully reversed flow conditions. A fixed incidence of 6 degrees is taken as a nominally attached-flow case, and agrees reasonably well with Isaacs' theory. A fixed incidence of 20 degrees is taken as a fully-separated case, and departs markedly from inviscid theory, and even more so from quasi-steady approximation. Experimental-computational comparison shows a computational overprediction of lift relative to experimental results, at moderate advance ratios. Agreement in fully reversed flow is, however, quite good.

**Conference Name:** AHS 71st Annual Forum

**Conference Date:** May 04, 2015

# Blade Sections in Streamwise Oscillations into Reverse Flow

**Anya Jones**

Assistant Professor

Department of Aerospace Engineering  
University of Maryland  
College Park, MD, USA

**Kenneth Granlund**

Research Engineer

Universal Technologies Corporation  
Wright-Patterson AFB, OH, USA

**Joachim Hodara**

Ph.D. Candidate

School of Aerospace Engineering  
Georgia Institute of Technology  
Atlanta, GA, USA

**Karen Mulleners**

Visiting Research Associate

Department of Aerospace Engineering  
University of Maryland  
College Park, MD, USA

**Marilyn Smith**

Professor

School of Aerospace Engineering  
Georgia Institute of Technology  
Atlanta, GA, USA

**Michael Ol**

Senior Aerospace Engineer

U.S. Air Force Research Laboratory  
Wright-Patterson AFB, OH, USA

## Abstract

A low-Reynolds number rectilinear analog of the retreating-blade problem is considered by computationally and experimentally studying a NACA0012 blade in spanwise oscillation in a free stream. Three-dimensional hybrid RANS-LES simulations with spanwise periodic boundary conditions and experimental flow visualization support the description of experimental direct force measurements for a wide range reduced frequencies and advance ratios, including fully reversed flow conditions. A fixed incidence of 6 degrees is taken as a nominally attached-flow case, and agrees reasonably well with Isaacs' theory. A fixed incidence of 20 degrees is taken as a fully-separated case, and departs markedly from inviscid theory, and even more so from quasi-steady approximation. Experimental-computational comparison shows a computational overprediction of lift relative to experimental results, at moderate advance ratios. Agreement in fully reversed flow is, however, quite good.

## Introduction

A major innovative thrust in rotorcraft is the extension and development of both high speed (above 250 knots) and environmentally-friendly vehicles. For conventional helicopters, the maximum speed has been limited to advance ratios ( $\mu = U_\infty/\Omega R$ ) at and below 0.5, due to the negative effects associated with the retreating blade. Designs that incorporate traditional, compound, or coaxial rotors (e.g., Cartercopter (Ref. 1) and the Sikorsky X2 Technology (Ref. 2)) may apply slowed rotational speeds to help achieve advance ratios that approach and exceed 1.0.

The consequence of the higher advance ratios, exacerbated with slowed rotation rates, is a rapid expansion of the region where reverse flow predominates. In the reverse flow region, the rotor blades operate with the trailing edge in the relative wind so that the blade operates more as a flat plate or bluff body rather than an airfoil. Reverse flow operation requires investigation and quantification to accurately capture these

physics as they influence the performance predictions. Figure 1 illustrates this increased region by comparing the reverse flow region for advance ratios of 0.5 and 1.0. The increase in the reverse flow area includes both inner and outer portions of the blade, spanning a large range of Reynolds numbers, and encompassing both incompressible and compressible flows.

Previously, at lower advance ratios, these very small reverse flow regions were less important in the overall understanding and prediction of the rotor behavior. Johnson et al. (Ref. 3), Harris (Ref. 4) and Ormiston (Ref. 5) invigorated research in reverse flow by highlighting their importance in future vertical lift design. High-advance-ratio research on rotating systems has demonstrated the complexity of the flow field. Since 2008, there have been three sets of high-aspect-ratio wind tunnel tests on a three-bladed NACA0012 rotor (Refs. 6, 7), four-bladed NACA0012 rotor (Refs. 8, 9) and the UH-60 four-bladed rotor (Refs. 10, 11), which have been included or been accompanied by computational analyses, for example, but not limited to, Refs. 9, 12, 13.

Beyond the rotor performance aspects, at these higher advance ratios, the reverse flow region can include large regions of radial flow, dynamic stall, and surge. Researchers have appropriately taken a *building block* approach to understand these various mechanisms in static and non-rotating dynamic situations prior to adding rotation. This approach has been proven to provide significant advances in understanding forward flight complex phenomena such as dynamic stall (see for example the collaborative efforts of the US, French and Germans in this area). If the physical mechanisms of each are not well-understood for simpler flight conditions in reverse flow, then incorrect modeling or physical conclusions may follow. With respect to radial or cross flow in the reversal region, Hodara and Smith (Ref. 14) and Bowen-Davies and Chopra (Ref. 13) have made advances to the state of the art in modeling and/or understanding the physics. Hodara and Smith, for example, have isolated and quantified the influence of cross flow on airfoil integrated quantities (lift, drag, moment) in reverse flow and developed new algorithms for comprehensive codes, reducing errors from 30 %–50 % to less than 10 %. In a recent collaborative effort, the University of Maryland (UMD) and the Georgia Institute of Technology (GIT) have partnered to quantify, both experimen-

tally and computationally, static and dynamic stall in reverse flow (Ref. 15). They have independently (Refs. 16, 17) obtained similar static solutions and have demonstrated that a reverse flow airfoil can be categorized into three distinct behaviors as angle of attack increases. Dynamically (with stall), the airfoil has five stages in the reverse flow cycle. Both static and dynamic behaviors in the reverse flow region are different than their forward flight counterparts, as described in Hodara et al. (Ref. 15).

This effort tackles the final major flow phenomenon of interest in reverse flow, referred to as surge, or the operation of rotor blades in oscillating flow fields. Contrary to dynamic stall, here the wing or rotor angle of attack may remain either constant or change, while the free-stream velocity oscillates. Greenberg (Ref. 18) and Isaacs (Ref. 19) pioneered the first efforts in this field for forward flight. For forward flight configurations, this topic has been investigated and reported in multiple sources, the most widely being Leishman (Ref. 20) and Harris (Ref. 21), which include both theory and computation. Harris notes that the addition of compressibility and viscosity (via high-fidelity computations) does not significantly change the magnitude of the lift, but does result in a translation of the lift mean value. Viscosity introduces a phase lag compared to incompressible theory. The physics associated with oscillating free-stream velocity has not been widely investigated for reverse flow conditions, although it may be important for new, innovative designs being proposed across the engineering disciplines, including rotorcraft. Initial assessment of water tunnel experiments, theory (Isaacs/Greenberg), and high-fidelity computations are examined to determine fundamental differences and areas where further research are needed, building on recent comparisons of theory and experiments (Ref. 22).

## Methodology

### Experimental Setup

The U.S. Air Force Research Laboratory's (AFRL) Horizontal Free-surface Water Tunnel, shown in Figure 2, is fitted with a three degree-of-freedom electric rig (Ref. 24), here used only in fore-aft translation of the test article via the surge motor. Motion is controlled via a Galil DMC-4040 motion controller from pre-programmed scripts, resulting in less than 0.1 mm linear and 0.2° angular position error. The test article, shown in Figure 3, is a 3D-printed ABS plastic NACA0012 airfoil with a chord of 100 mm and span of 457 mm, leaving a nominally 0.5 mm wide gap between each wingtip and the test section wall. The model is reinforced along the span internally with two 6.5 mm diameter carbon fiber tubes. The blade is installed upside down in the water tunnel so that positive lift acts downwards in Figure 3.

Flowfield visualization was performed using dye-illuminated planar laser fluorescence. A high concentration of Rhodamine 6G in water was injected at the leading and trailing edges at 3/4-span. Dye flow rate was controlled by a positive-displacement pump, connected to a set of 0.5 mm internal-diameter rigid lines glued to the surface of the plate

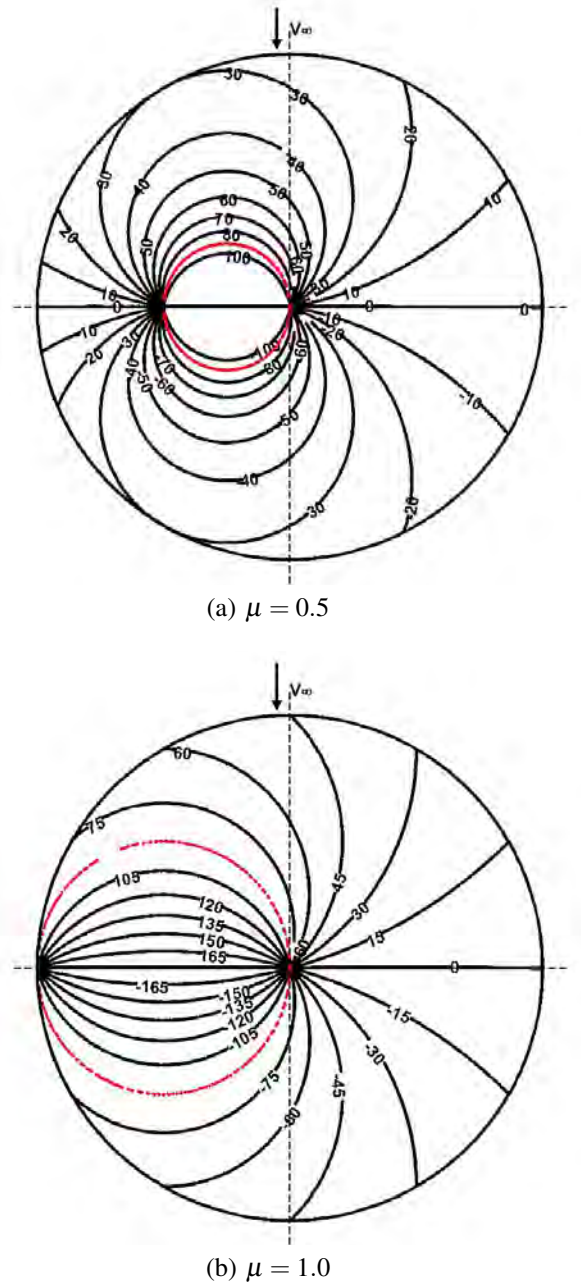


**Fig. 1. Iso-sweep angles [deg] over the rotor disk at  $\mu = 0.5$  and 1.0 (counter-clockwise rotation). The red line indicates the reverse flow region (Ref. 23).**

as documented by (Ref. 24). The dye was illuminated by an Nd:YLF 527 nm pulsed laser sheet of 2 mm thickness at 50 Hz, and images were recorded with a PCO DiMax high-speed camera through a Nikon PC-E 45 mm Micro lens. A Tiffen orange 21 filter was used to remove the incident and reflected laser light, leaving only dye fluorescence.

Force measurements were performed using a submergible ATI Nano25 IP68 6-component strain gauge force/torque sensor, sampled at 100 Hz with a hardware low-pass filter at 34 Hz, and then it was filtered at 5 times the motion frequency using a 4th-order Chebyshev II low-pass filter in Matlab. All motions were repeated for one hundred cycles; the first three

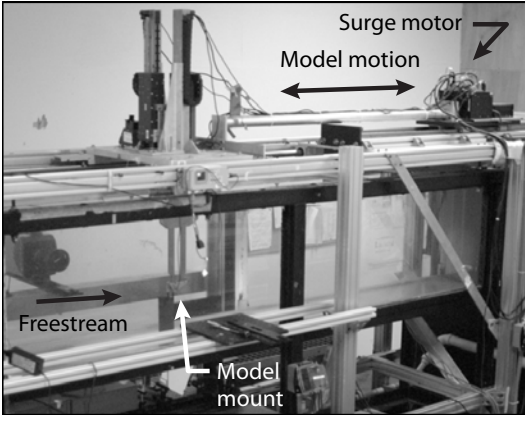


**Fig. 2. AFRL free-surface water tunnel test section with planar motion mechanism.**

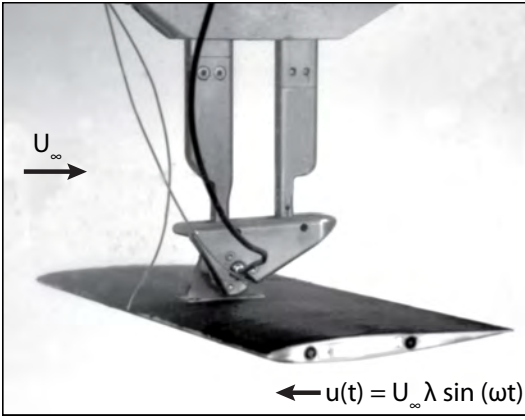


**Fig. 3. NACA0012 airfoil installed in the AFRL free-surface water tunnel.**

cycles were not included in the ensemble averages given here to remove transients. In all of the plots below, time has been nondimensionalized by the motion period  $T$ , while  $C_l$  has been nondimensionalized by the free stream in the water tunnel,  $U_\infty$ .

### Blade Kinematics

In the current work, a rotating rotor blade has been modeled as a two-dimensional blade element in harmonic motion. Neglecting inflow and flapping, the relative flow over a blade element of a rotor in hover is given by  $U = \Omega r$ , where  $\Omega$  is the angular velocity of the rotor blade and  $r$  is the radial location of the blade element. For a rotor in forward flight, the addition of a relative free stream,  $U_\infty$ , introduces a harmonic oscillation and the incident flow over a blade element becomes

$$U(\psi) = \Omega r + U_\infty \sin \psi = \Omega r + \mu \Omega R \sin \psi \quad (1)$$

where  $\mu = U_\infty / \Omega R$  is the advance ratio and  $R$  is the rotor radius. Equation 1 is plotted in Figure 4, where the azimuthal position of the blade (i.e.,  $0^\circ \leq \psi \leq 360^\circ$ ) is mapped to a nondimensional time scale  $t/T$ . The maximum relative flow  $U_{\max} = U_\infty + \Omega r = \Omega(r + \mu R)$  occurs at a blade azimuthal angle of  $\psi = 90^\circ$ , corresponding to  $t/T = 0.25$ . The minimum

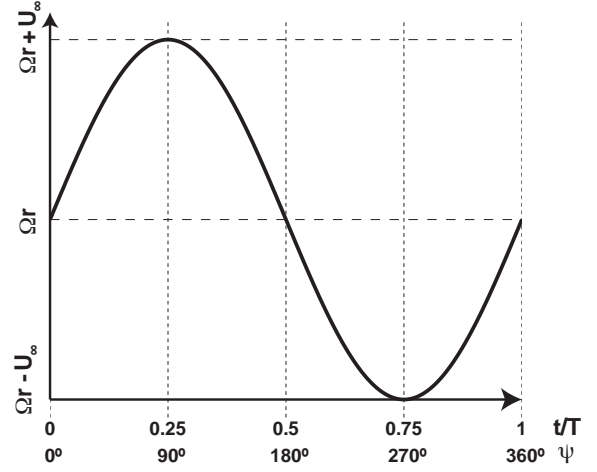


**Fig. 4. Normalized velocity during one rotor cycle.**

relative flow  $U_{\min} = U_\infty - \Omega r = \Omega(r - \mu R)$  occurs at a blade azimuthal angle of  $\psi = 270^\circ$ , corresponding to  $t/T = 0.75$ . The amplitude of the oscillation of the relative flow experienced by a blade element is the free stream,  $U_\infty$ , and the mean velocity at radial position  $r$  is  $\bar{U} = \Omega r$ .

To model the rotational motion as rectilinear motion, the amplitude of the velocity oscillation is nondimensionalized by the local mean velocity to define a blade-element advance ratio

$$\lambda(r) = \frac{U_\infty}{\Omega r} = \frac{\mu}{r/R} \quad (2)$$

where  $R$  is the rotor radius,  $\mu = U_\infty / \Omega R$  is the advance ratio of the rotor, and  $\lambda$  is a parameter that characterizes the local (radial) magnitude of reverse flow. When  $r = R$ ,  $\lambda = \mu$ , and when  $r < R$ ,  $\lambda > \mu$ . Blade elements inboard of the blade tip experience more extreme reverse flow than does the blade tip. For example, if  $\mu = 1$ , then  $\lambda = \mu = 1$  at the blade tip ( $r/R = 1$ ). At the mid-span, however,  $r/R = 0.5$  and  $\lambda = 2\mu$ . In this case, the most severe reverse flow experienced at the tip of the rotor blade is a relative velocity of zero, while the mid-span experiences a reverse flow that is twice the free stream.  $\lambda$  also characterizes the radial extent of reverse flow for a given value of  $\mu$ , as illustrated in Fig. 3. For example, if  $\mu = 0.5$ ,  $\lambda > 1$  for  $r/R < 0.5$ . Regions of the blade inboard of  $r/R = 0.5$  will experience reverse flow.

To produce a harmonic oscillation in rectilinear motion analogous to that experienced by the rotating blade element, the blade mounted in the water tunnel was driven forward and aft in a steady free stream of speed  $U_\infty$  with a velocity profile of

$$u'(t/T) = U_\infty \lambda \sin(\omega t/T) \quad (3)$$

where  $\omega$  is the angular frequency of the nondimensional time scale,  $t/T$ . Note that  $u'(t)$  is the speed at which the model is driven and varies from  $-U_\infty$  to  $+U_\infty$  for  $\lambda = 1$ . In the water tunnel, the harmonic oscillation driven by the surge motor represents the forward-flight contribution to velocity. The unsteady flow incident to the blade element is computed by adding the component from the rotation of the rotor such that

$$u(t/T) = \omega r + U_\infty \lambda \sin(\omega t/T) = U_\infty [1 + \lambda \sin(\omega t/T)] \quad (4)$$

**Table 1. Test matrix.** Force histories are available for all of the cases listed. Dye flow visualization and numerical simulations at  $\theta = 20^\circ$  are available for the cases in *italics*.

Reduced frequency $k = \pi f c / U_\infty$	Blade-element advance ratio $\lambda = (2\pi A f / U_\infty) = 2Ak/c$
0.0952	0.57, 0.71, 0.86, 1.00
0.1111	0.67, 0.83, 1.00, 1.17
0.1333	0.80, 1.00, 1.20, 1.40
0.1667	1.00, 1.25, 1.50, 1.75
0.2222	1.33, 1.67, 2.00, 1.75

Note that in the water tunnel, the free stream  $U_\infty$  represents the velocity due to blade rotation, and so  $U_\infty = \omega r$ . If  $\lambda = 1$  as in the previous example, the blade element experiences a *relative flow* ranging from 0 to  $2U_\infty$ .

The position of the blade element in the driven rectilinear harmonic motion,  $s(t)$  is given by the integral of the velocity profile in Eq. 3,

$$s(t/T) = -\frac{U_\infty \lambda}{\omega} \cos(\omega t/T) \quad (5)$$

The physical frequency of the blade position,  $f = \omega/(2\pi)$ , can be written in terms of the reduced frequency,  $k = \omega c/2U_\infty$ , as

$$f = kU_\infty/\pi c \quad (6)$$

and the amplitude of the blade motion as

$$A = \frac{U_\infty \lambda}{\omega} = \frac{\lambda c}{2k} \quad (7)$$

Thus, for a fixed blade chord  $c$  and free stream  $U_\infty$ , the parameter space is defined by the blade-element advance ratio  $\lambda$  and the reduced frequency  $k$ .

Experiments were performed in water at a constant Reynolds number of  $Re = U_\infty c/\nu = 40000$ , thereby fixing the value of  $U_\infty$ . The amplitude of the blade motion was limited by the 0.6 m stroke length of the surge motor. The reduced frequencies tested,  $0.095 \leq k \leq 0.222$ , were limited by the capabilities of the force balance. The experimental parameter space in  $k$  and  $\lambda$  is given in Table 1 and illustrated in Fig. 5. Experiments were run with the NACA0012 blade mounted at an angle of incidence of  $\theta = 6^\circ$  and  $20^\circ$  to assess behavior in nominally attached and separately conditions, respectively.

## Numerical Methods

A numerical solver has been developed at GIT to study unsteady problems such as dynamic stall and rotor blades in reverse flow. This new platform was specifically designed to rapidly implement and evaluate state-of-the-art algorithms, including turbulence and transition approaches. The three-dimensional compressible governing equations are solved in a time-accurate manner using a cell-centered finite volume approach on structured grid topologies. The spatial reconstruction is carried out using Van Leer's MUSCL scheme,

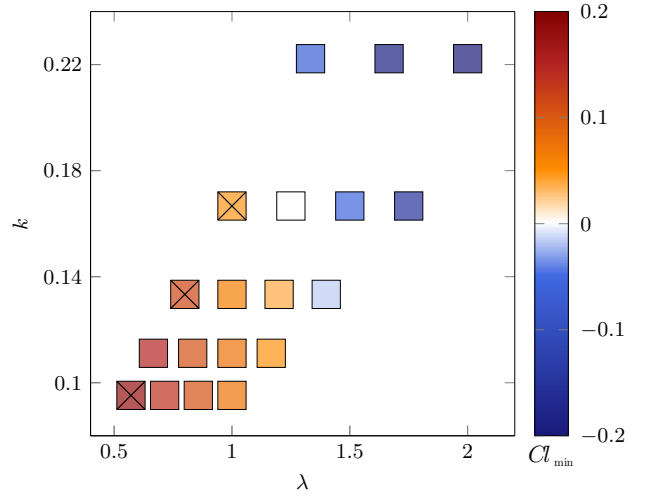


**Fig. 5. Text Matrix in the  $k - \lambda$  parameter space, with symbols colored to represent  $Cl_{\min}$  for a blade at  $\theta = 6^\circ$ . Symbols represent points in the parameter space at which force data was acquired for both  $\theta = 6^\circ$  and  $20^\circ$ . Symbols marked with an 'x' represent cases for which dye flow visualization and numerical simulations were also performed (for  $\theta = 20^\circ$ ).**

leading to second-order accuracy. The convective fluxes are computed using Roe's flux difference splitting scheme, while the viscous fluxes are obtained from second-order central differences. The solution is marched in time using the implicit LU-SSOR scheme combined with the method of Gear to achieve second-order temporal accuracy. The number of Newton sub-iterations at each physical time step is chosen to ensure a proper convergence of the residuals. A large number of boundary conditions has been implemented, including inviscid/viscous walls, non-reflecting inlets/outlets based on Riemann invariants, etc. The solver is fully parallel (MPI) and includes rigid body rotation/translation using the Arbitrary Lagrangian Eulerian approach (Ref. 25). In the present study, the turbulent equations are solved in a loosely coupled manner using the hybrid Reynolds-Averaged Navier Stokes - large eddy simulation (HRLES) model of Sanchez-Rocha (Ref. 26). Validation of the code has been verified over a large number of test cases, ranging from turbulent circular cylinders to oscillating wings in reverse flow, several of which are illustrated in Hodara et al. (Ref. 15).

In the current work, numerical simulations were performed on a semi-infinite NACA0012 blade at an angle  $\theta = 20^\circ$  with respect to the free stream. Grid motion reproduced selected cases from the experimental test matrix, each with an oscillation amplitude  $A/c = \lambda/(2k) = 3$ . Maintaining this constant amplitude, three cases of different reduced frequency were evaluated:  $k = 0.167, 0.133$  and  $0.095$ . Fixing the amplitude of the motion and the reduced frequency,  $\lambda$  becomes 1.0, 0.8, and 0.57, respectively, for the three cases. Figure 5 illustrates where these cases lie in the parameter space explored in the current work. The  $\lambda = 1.0$  case is of particular interest because the relative velocity in a blade-element-fixed reference frame reaches zero at  $t/T = 0.75$ , corresponding to the onset



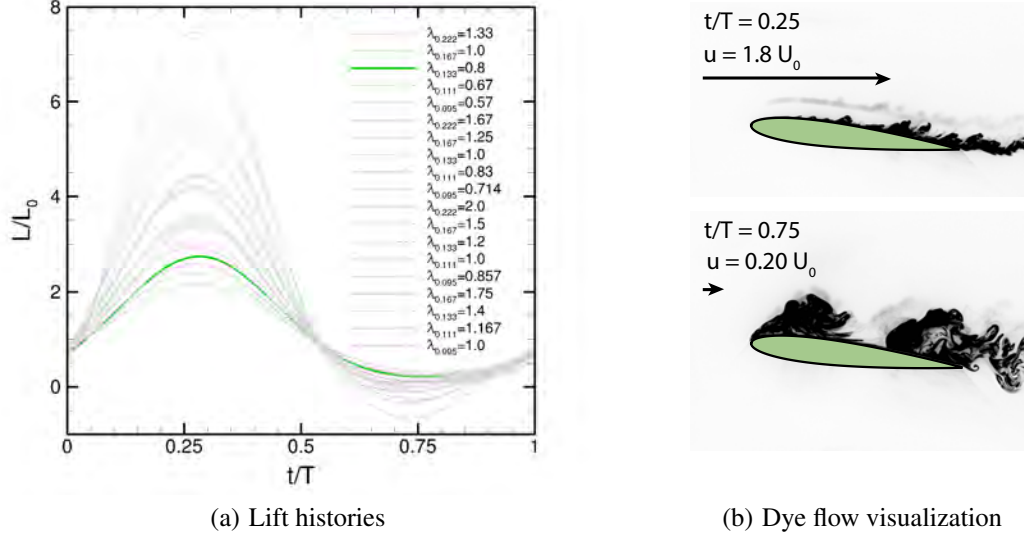


**Fig. 6. Experimental results for a NACA0012 at  $\theta = 6^\circ$ . Dye flow visualization is shown for  $\lambda_{0.1333} = 0.8$ .**

of reverse flow.

The experimental test conditions discussed previously were reproduced in the numerical simulations. The Reynolds number based on the airfoil chord is  $Re_c = 40000$  and the free-stream Mach number is  $M_\infty = 0.1$ . This Mach number does not correspond to the experimental value ( $M_\infty < 0.001$ ) due to the density-based nature of the solver and the current absence of a low Mach number preconditioner. The Reynolds number and unsteady characteristics were scaled to reproduce the experiment given the change in Mach number. The change in density was found to remain consistently below 4 % when the dynamic pressure was maximum (case  $\lambda_{0.167} = 1.0$  at  $t/T = 0.25$ ). It is therefore expected that compressible effects will be negligible in the present study based on aerodynamic theory.

The physical time step was maintained for all three cases evaluated numerically, with a flow particle taking approximately 1250 time steps to travel from the leading edge to the trailing edge of the airfoil. Based on the oscillation periods of the three cases, the number of time steps per cycle is 25000, 30000 and 40000 for  $\lambda = 1.0$ , 0.8 and 0.57 respectively. All simulations included the HRLES turbulence closure, and the results were phase-averaged over 12, 7, and 5 cycles for the three respective cases. The number of cycles becomes small for lower values of  $\lambda$ , but smaller  $\lambda$  coincides with smaller fluctuations in forces and moments from cycle to cycle, which mitigates the need for ensemble averaging over large numbers of cycles. Due to the fine time steps employed in the simulations, 5 Newton subiterations were sufficient for reducing the  $L^\infty$  norm of the residuals by two orders of magnitude between each physical time step. A temporal analysis concluded that increasing the number of subiterations further had a negligible impact on the results, similar to prior conclusions by Liggett and Smith (Ref. 27).

### Computational Grid

A rigorous grid refinement study was conducted to identify the optimal mesh for the present configuration; a family of O-grids was generated following the guidelines of Spalart (Ref. 28) and Smith et al. (Ref. 16). The spacing at the wall was chosen to ensure that  $y^+ < 1$  in the first cell, with approximately 50 points resolving the boundary layer. The number of points in the circumferential direction was increased from 499 for the coarse grid to 999 for the fine grid, while the number of grid points in the wall normal direction was increased from 161 to 201. The computational domain extends approximately 50 chord-lengths from the blade section in all directions. The radial or spanwise dimension of the domain must be carefully chosen to ensure that the periodic boundary conditions do not impact the flow field in three-dimensional simulations. Most researchers (Refs. 29–31) have used a width of  $1 \times c$  to simulate the flow past a semi-infinite wing in post-stall conditions, while Smith (Ref. 16) used a larger width of  $2 \times c$ . In the present study, the coarsest grid has a width of  $1 \times c$ , which is extended to  $2 \times c$  for the finest mesh. In all cases, the radial aspect ratio is held constant, with 31 points per chord length ( $z^+ \simeq 200$  at the Reynolds number considered). This gridding approach was found to generate accurate (when correlated with water and wind tunnel experimental data) static and dynamic simulations in forward and reverse flow conditions, as demonstrated by Smith et al. (Ref. 16) and Hodara et al. (Ref. 15).

Several meshes were evaluated in the simulation of the flow past a semi-infinite static NACA0012 wing at  $Re_c = 1.1 \times 10^5$ , deep into the reverse stall regime ( $\alpha = 150^\circ$ ). This challenging configuration was computed using the HRLES turbulence closure, with approximately 5000 time steps resolving each vortex shedding cycle. Lift and drag coefficients, as well as Strouhal number were captured within 3 % of one

another for the two meshes identified here. The solution obtained with the coarser mesh ( $499 \times 31 \times 161$  over a single chord-width span dimension) is considered sufficient and applied in the present study.

## Results and Discussion

Experiments were performed on a NACA0012 blade mounted at  $\theta = 6^\circ$  and  $20^\circ$  incidence over a wide  $k - \lambda$  parameter space, given in Table 1 and Figure 5. Numerical simulations were performed on a semi-infinite NACA0012 wing at an incidence angle of  $\theta = 20^\circ$ . Of particular interest is the transition from forward to reverse flow that exists at  $\lambda = 1.0$ , where the relative velocity in a blade-element-fixed reference frame reaches zero at  $t/T = 0.75$ . The two incidence angles were selected to provide one case expected to be free of significant flow separation suitable for comparison with inviscid theory, and one case more representative of the separated flow likely to exist in the reverse flow region of a rotor disk.

### Results at Low Incidence

Figure 6(a) gives the experimentally measured phase-averaged lift coefficient as a function of nondimensional time for the NACA0012 blade at  $\theta = 6^\circ$ . The lift coefficient is based on the free stream condition independent of the oscillatory motion, i. e.,  $C_L = 2L/(\rho U_0^2 S)$  where  $U_0$  is the tunnel freestream and  $S$  is the wing area. The lift coefficient history is shown in the figure as the instantaneous unsteady lift coefficient  $C_L$ , normalized by the static lift coefficient as measured at  $\theta = 6^\circ$ ,  $C_{L_0} = 0.57$ . Because both the unsteady and static lift coefficients are based on the free stream velocity of the water tunnel,  $C_L/C_{L_0} \equiv L/L_0$ . Note that in the following text and figures, the subscripts on  $\lambda$  are the value of  $k$  for that case. For example,  $\lambda_{0.222} = 1.33$  refers to a case where  $\lambda = 1.33$  and  $k = 0.222$ .

Force curves are shown in Figure 6(a) for each of the cases evaluated, with the one corresponding to the dye flow visualization in Figure 6(b) highlighted in green. In each case, lift rises as the blade surges into the free stream and the relative flow increases. The maximum relative velocity occurs at  $t/T = 0.25$ , and the maximum lift occurs just past this point, at  $t/T = 0.28$ . Lift decreases as the blade retreats and, for most cases, remains near zero for a substantial portion of the retreating phase of the motion cycle. Dye flow visualization of the  $\lambda_{0.1333} = 0.8$  case is shown in Figure 6(b) at  $t/T = 0.25$  and  $0.75$ . At  $t/T = 0.25$ , the blade is advancing into the free stream, while the blade is retreating at  $t/T = 0.75$ . As  $\lambda < 1.0$ , the blade section does not experience reverse flow. The relative flow vectors,  $u$ , are shown to scale in the figure. At this incidence angle, flow is attached to the blade during the advancing phase, though incipient separation is observed at  $t/T = 0.75$ , where the relative flow velocity is lowest.

In a few cases shown in Figure 6(a), lift becomes negative during the retreating phase (See also Fig. 5). The largest negative lift is produced by the  $\lambda_{0.222} = 2.0$  case, followed

by  $\lambda_{0.222} = 1.67$  and  $\lambda_{0.167} = 1.75$ . A small amount of negative lift is produced by the  $\lambda_{0.222} = 1.33$  and  $\lambda_{0.167} = 1.5$  cases. Negative lift was only observed for cases where  $\lambda$  is significantly greater than 1. Here, the relative flow direction reverses and the blade experiences flow from the geometric trailing edge to the geometric leading edge (i.e., right to left in Figure 6(b)). In this orientation, a blade that was at a positive angle of attack is now at a negative angle of attack and so the direction of lift reverses.

### Results at High Incidence

**Numerical Flow Visualization** Numerical simulations at  $\theta = 20^\circ$  provide instantaneous flow fields throughout the blade motion, demonstrating the evolution of the flow structure. Two-dimensional slices of the flow field were extracted at various times during the cycle to investigate the flow physics of the various cases. These slices were taken during a single (last) cycle at the midspan location and have not been ensemble-averaged. Contours of vorticity magnitude are shown in Figures 7 and 8 at eight instances during the blade motion for three cases. Note that since  $A/c = \lambda/(2k) = 3$  is constant for the three cases shown here, the reduced frequency of the motion increases with  $\lambda$ .

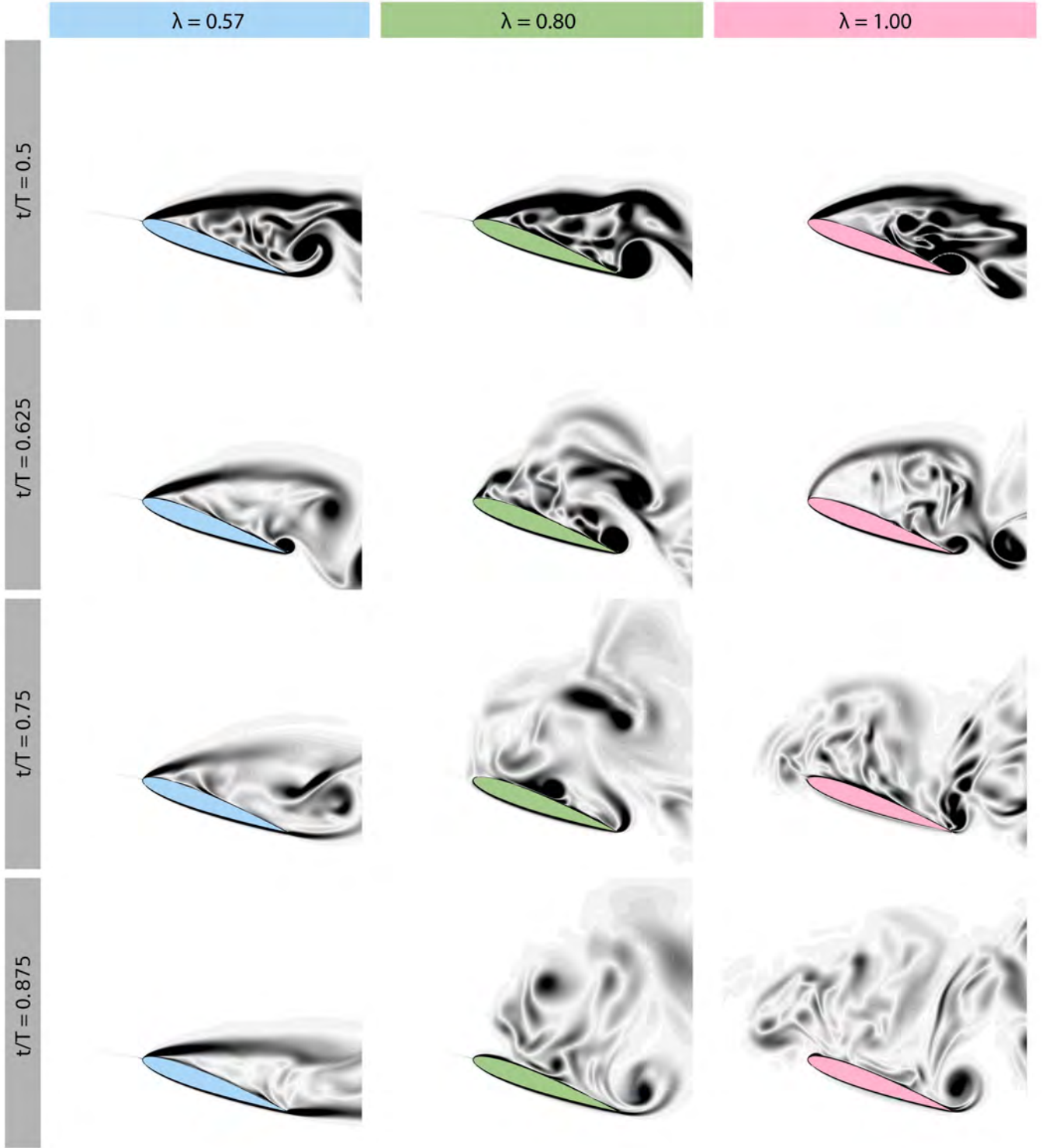
The beginning of the cycle,  $t/T = 0$ , is defined as the instant when the blade section is the furthest downstream and the oscillatory velocity is equal to zero (see Fig. 4). The relative flow velocity at this instant is thus equal to the free stream. It can be seen in row 1 of Figure 7 that the flow structure at this point in time differs significantly from that over a static wing, and varies with reduced frequency of the motion. In the case where  $\lambda = 0.57$ , the flow is separated from near the leading edge, much like a static airfoil at such high incidence. As the reduced frequency increases, however, dynamic effects become more pronounced and the flow remains attached over a large portion of the suction side of the blade. The physical explanation for this boundary layer reattachment becomes apparent at the end of the cycle. Moving forward in time, the blade accelerates into the free stream and reaches its maximum relative velocity when  $t/T = 0.25$  (row 3 of Fig. 7). At this time, the flow features are similar for all three cases, though the shear layer appears to be less stable at  $\lambda = 0.8$  than in the other cases. In all three cases, the boundary layer separates close to the leading edge and a large region of separated flow and thus low pressure exists on the suction side of the airfoil. These effects, combined with the large dynamic pressure on the pressure side, yield lift forces up to 8 times the static value (for  $\lambda = 1.0$ ), as shown in Figure 12.

In the second half of the cycle, the blade decelerates to  $t/T = 0.5$ , where the oscillation velocity approaches zero and the freestream speed is recovered. The flow fields at this point are given in row 1 of Figure 8. The shear layer originating at the leading edge extends away from the blade surface at an angle dependent on the blade-element advance ratio  $\lambda$ . The variation in the shear layer angle is barely perceptible in these images at  $t/T = 0.5$ , but becomes much more significant as the blade section begins its retreating phase, shown in row 2 of





**Fig. 7. Numerically-generated instantaneous vorticity magnitude contours on a NACA0012 blade section at  $Re = 40000$ ,  $\theta = 20^\circ$  for  $0 \leq t/T < 0.5$ . The three cases shown here are for oscillations defined by  $\lambda_{0.095} = 0.57$ ,  $\lambda_{0.133} = 0.8$ , and  $\lambda_{0.167} = 1.0$ .**



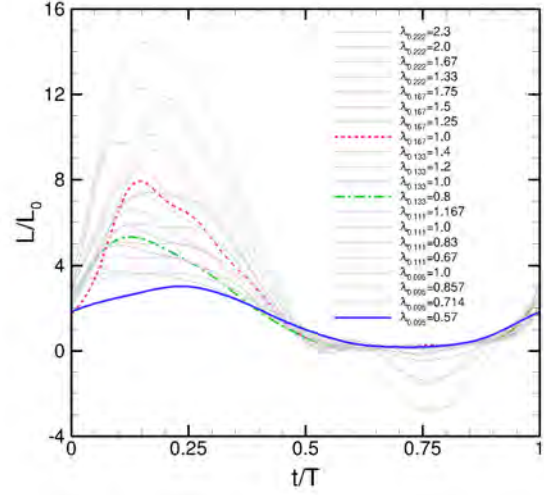
**Fig. 8.** Numerically-generated instantaneous vorticity magnitude contours on a NACA0012 blade section at  $Re = 40000$ ,  $\theta = 20^\circ$  for  $0.5 \leq t/T < 1.0$ . The three cases shown here are for oscillations defined by  $\lambda_{0.095} = 0.57$ ,  $\lambda_{0.133} = 0.8$ , and  $\lambda_{0.167} = 1.0$ .

Figure 8. At  $t/T = 0.625$  the leading edge shear layer breaks down for both  $\lambda = 0.80$  and  $1.0$ , and a low velocity turbulent region appears on the suction side of the airfoil. This breakup occurs earlier for  $\lambda = 0.8$  than for  $\lambda = 1.0$  due to the more unstable shear layer in the former case, and may be related an effect of reduced frequency. Remember that in the current set of experiments, the amplitude of the blade motion was fixed, so both the blade-element advance ratio  $\lambda$  and reduced frequency  $k$  vary together.

At  $t/T = 0.75$  (row 3 in Fig. 8), the shear layer extending downstream from the leading edge persists at  $\lambda = 0.57$ . At higher reduced frequencies, the turbulent wake front moves slightly upstream of the airfoil. This is initially counter-intuitive since the relative velocity in the body frame does reach zero at  $\lambda = 1$  and  $t/T = 0.75$ , but does not become negative at any time. However, note that the blade section is retreating and so flow structures that advect more slowly than the freestream will appear to move upstream relative to the blade section. The numerical flow visualization comports well with experimental flow visualization (see Fig. 10).

Finally, at  $t/T = 0.875$  (shown in row 4 in Fig. 8), the boundary layer begins to reattach at the leading edge of the blade as the relative flow velocity increases once again. This is most evident in the  $\lambda = 0.57$  case where the incident flow has remained of the largest magnitude. In this case, the shear layer separation angle remained relatively small throughout the cycle and the turbulent wake did not reach the leading edge of the airfoil. Throughout the cycle, structure of the flow field for this case remained more similar to that of a static airfoil than did those at higher blade-element advance ratios. At low  $\lambda$ , variations in the incident flow velocity are small enough that the overall flow structure is not fundamentally changed as the blade advances and retreats in the free stream. At higher  $\lambda$ , larger variations in incident flow velocity have resulted in very low flow velocities and near-stagnant flow as the blade retreats. When the blade then reverses direction and begins the cycle again, there is a small window of time in which an attached boundary layer forms (over at least part of the blade section) in this near-stagnant flow before flow separation once again occurs.

The case of  $\lambda = 0.8$  serves to further illustrate how the flow behaves between large separation ( $\lambda = 0.57$ ) and attached flow ( $\lambda = 1.0$ ) at time  $t/T = 0.0$ . As the cycle progresses, the instability that lies at  $\lambda = 0.8$ , between the two starting extremes, becomes obvious. As the cycle approaches its midpoint ( $t/T = 0.5$ ), the reverse flow from the leading edge shear layer and trailing edge vortex interaction has penetrated closest (of the three  $\lambda$  configurations) to the leading edge. For  $\lambda = 0.8$ , the leading edge shear layer angle maintains a trailing edge vortex that is stronger and closer to the airfoil trailing edge. By  $t/T = 0.625$ , the middle  $\lambda = 0.8$  case is striking with its unstable shear layer. It then breaks down differently than at advance ratios greater and less than this value. This instability can have significant impact on the behavior of the rotor blade when combined with angular motion, and could partially explain why some airfoil and rotor configurations in



**Fig. 9. Experimental lift histories for a NACA0012 blade section at  $\theta = 20^\circ$ .**

the literature appear to be more sensitive during dynamic stall than others.

**Experimental Results** Experimental results at  $\theta = 20^\circ$  are given in Figures 6(a) and 10. The force histories have a shape similar to that observed at  $\theta = 6^\circ$ , with lift rising as the blade surges into the freestream and dropping to near zero as the blade retreats. At this high angle of attack, however, maximum lift no longer lags the maximum dynamic pressure. The maximum lift recorded during the experiments appears to lead the blade motion, and more so as  $\lambda$  increases. While counter-intuitive, similar phase-lead behavior has been previously observed at  $0.1 < k < 0.6$  for a NACA0009 at  $\lambda = 0.1$  (Ref. 22).

Experimental flow visualizations are available for the current experiments at  $t/T = 0.25$ , given in Figure 10). These images exhibit many of the same flow features observed in the numerical simulations. The angle of flow separation evident in the dye flow visualization at  $t/T = 0.75$  is drastically different for the three cases as was observed in the numerical results. It should be noted that the large vortex visible upstream of the leading edge in the dye flow visualization at  $\lambda = 1$  was also predicted in the numerical simulations, albeit at a later time of  $t/T \approx 0.87$ . This vortex is an artifact of the leading-edge shear layer rolling up as the blade retreats. Despite obvious differences in the structure of the separated flow across the three cases shown here, the flow is fully separated in each case and the blade produces near-zero lift at  $t/T = 0.75$ .

Figure 11 gives the lift histories for four different cases in which  $\lambda = 1$  is fixed and the reduced frequency  $k$  (and thus the amplitude of the motion,  $A/c$ ) is varied. The curves shown here are a subset of those given in Figure 6(a). Although the maximum lift achieved in these cases varies in magnitude, the rate at which lift builds up over  $0 < t/T < 0.1$  and falls off over  $0.25 < t/T < 0.5$  is similar. In the second half of the cycle,  $0.5 < t/T < 1$ , the magnitude of lift agrees as well.

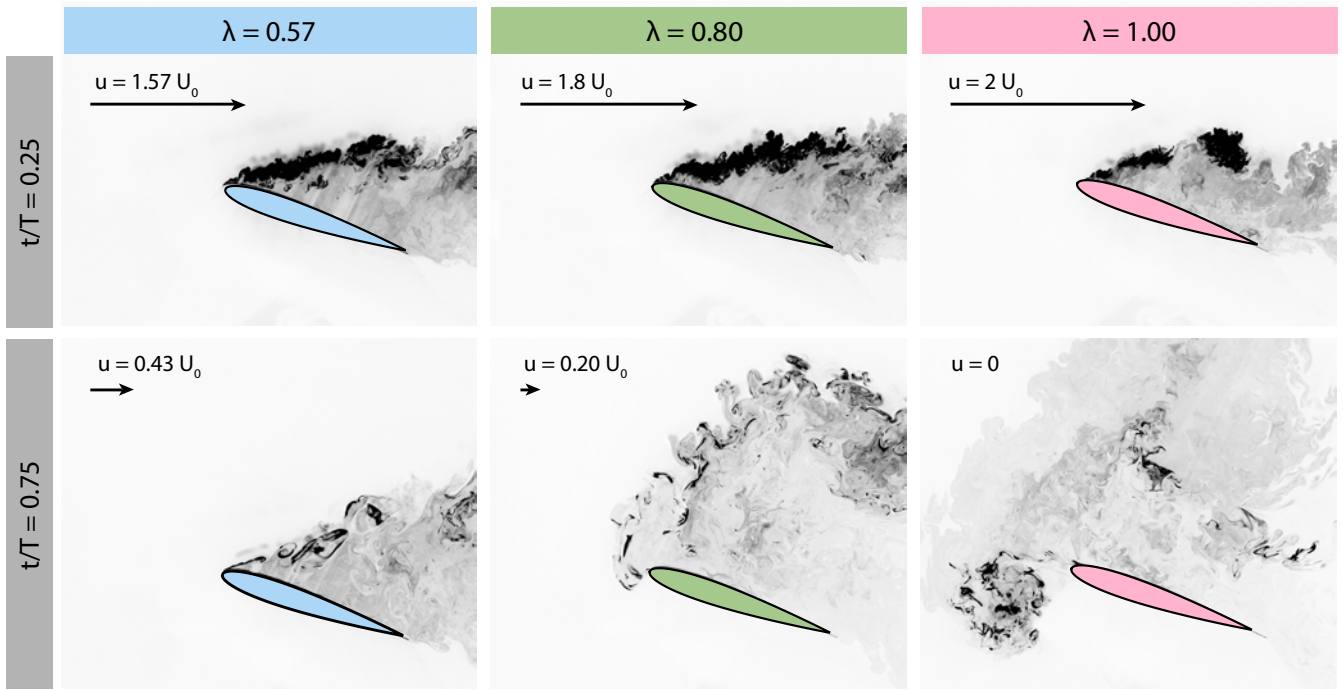


Fig. 10. Experimental dye flow visualization for a NACA0012 blade section at  $\theta = 20^\circ$ .

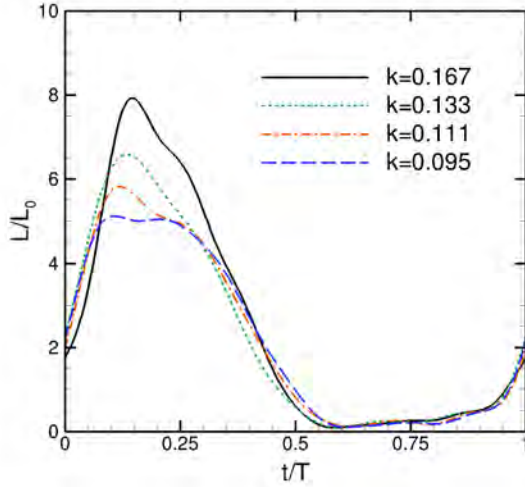


Fig. 11. Lift histories for a fixed  $\lambda = 1.0$  and varying  $k$ .

It should be noted that the normalized apparent mass contribution to lift,  $L_a/L_0$ , is proportional to the product of blade-element advance ratio  $\lambda$  and reduced frequency  $k$ . In the cases presented in this paper, apparent mass is a negligible contributor. The difference in peak normalized lift  $t/T = 0.25$  in Figure 11 for varying reduced frequency  $k$  at constant  $\lambda = 1.0$ , must therefore come from a difference in circulation and vortex advection speed from the preceding retreating phase.

### Comparison of Integrated Forces

The lift histories as computed numerically, measured experimentally, and predicted by inviscid theory are summarized in Figure 12. In this figure, all of the lift histories are normalized as described previously, i.e., by the viscous static lift,  $L_0$ . For all cases the broadest variations and the most interesting phenomena in force-histories occur on the advancing semi-stroke, especially between  $t/T = 0$  and  $t/T \sim 0.3$ .

Inviscid theory does a reasonable job of predicting unsteady lift at  $\theta = 6^\circ$  (Fig. 12(a)), though lift is overpredicted during the first half of the stroke. The theoretical model by Isaacs (Ref. 19) is sufficient to predict lift history because the flow is largely attached and falls within the limitations of the potential flow assumptions from which this theories was derived. This is not the situation at  $\theta = 20^\circ$  incidence (Fig. 12(b)) where viscous effects relating to flow separation predominate. Consequently, Isaacs' model grossly overpredicts peak lift for all cases at high incidence and does not account for the viscous interactions that lead to a phase lead of the peak lift.

At  $\theta = 20^\circ$  (Fig. 12(b)), computations predict similar trends relative to the Isaacs model but give a better estimate of the peak lift. For  $\lambda = 0.8$ , the peak lift measured experimentally is well-predicted by the numerical simulations, for  $\lambda = 1.0$  it is slightly underestimated, and for  $\lambda = 0.57$  it is largely overestimated. Comparing computational flow fields and flow visualization for  $t/T = 0.25$  reveals more distinct large-scale structures as a result of the roll up of the shear layer in the computational results than in the experiments. The presence of more coherent vortical structures above the airfoil leads to an increased (and in this case overpredicted) lift.



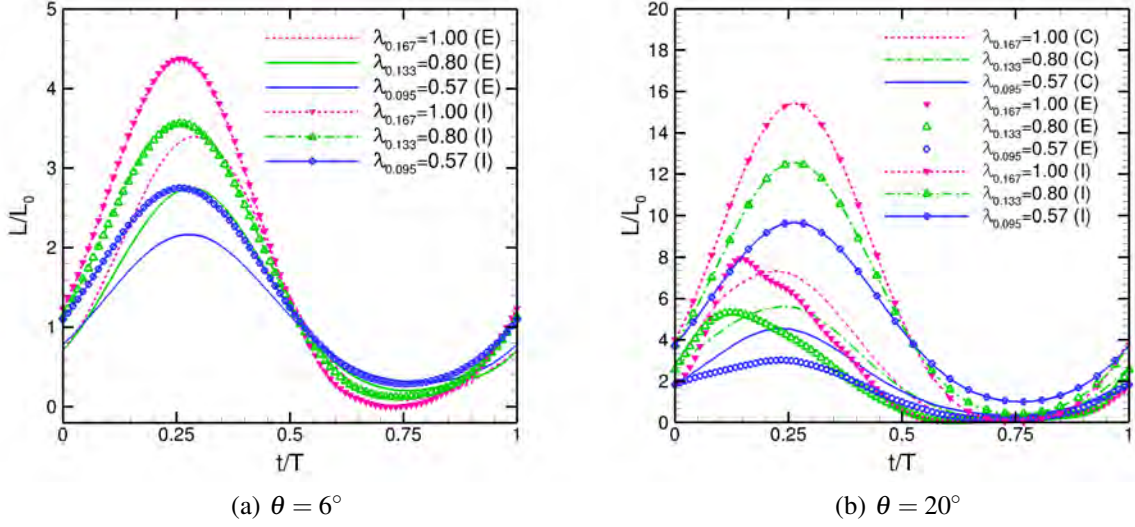


**Fig. 12. Force history comparison between numerical simulations, experiments, and theory.**

Furthermore, the computations do not predict the phase lead of the experimental lift histories with regard to the motion. With increasing  $k$  or  $\lambda$ , maximum lift no longer coincides with maximum dynamic pressure (at  $t/T = 0.25$ ) as predicted by the inviscid model, but occurs earlier in the period. For these cases, the velocity relative to the wing is larger and therefore the vorticity production that is fed into the shear layer is greater, leading to a steeper rise in lift, a larger peak lift, and stronger viscous interaction in the shear layer early in the advancing phase of the cycle. As the cycle progresses, stronger viscous effects might cause precipitation of deep stall, a weakening of bound circulation, and a drop in lift ahead of the drop in dynamic pressure.

Note that normalized lift at  $\theta = 20^\circ$  and  $t/T = 0$  is near 2, and not near 1. Dynamic pressure at  $t/T = 0$  and  $t/T = 0.5$  is just the free-stream value, so a quasi-steady lift response in this normalization at those phases would be 1. Also, quasi-steady lift would be maximum at  $t/T = 0.25$ , where the instantaneous dynamic pressure is maximum. In the computation this is approximately true, but in the experiment the lift peaks before  $t/T = 0.25$ , i.e., at a lower instantaneous dynamic pressure. It is conjectured that this could be due to the partial reattachment of the suction-side flow shortly after  $t/T = 0$ . As the blade section accelerates into the free stream, suction is progressively attenuated, and thus the lift (and also the drag; or more properly, the normal-force) will peak before reaching maximum dynamic pressure.

The extent to which lift history departs from the quasi-steady can be further elucidated by calculating lift not with respect to the steady free-stream dynamic pressure, but with respect to the instantaneous value of dynamic pressure, obtained from superimposing the surging speed of the blade and the free stream speed of the tunnel. These results are presented in Figure 13. In this formulation, a truly quasi-steady response would be identically 1 for all  $t/T$ , even in the case

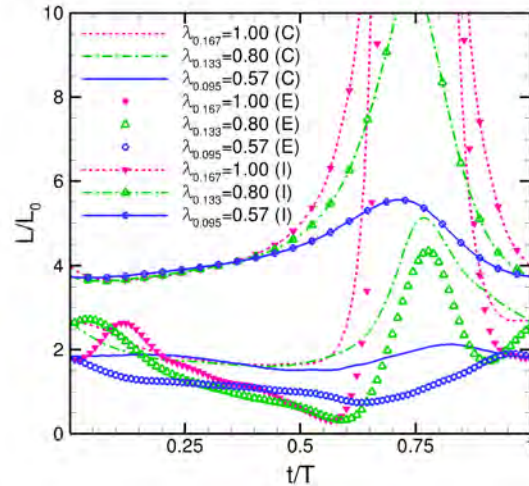


**Fig. 13. Lift history normalized with respect to the instantaneous value of dynamic pressure.**

of  $\lambda = 1$  at  $t/T = 0.75$  (zero lift produced at zero dynamic pressure, or 0/0). It was already mentioned that at  $t/T = 0$ , the measured and computed lift are near 2, and the measured lift peaks occur before  $t/T = 0.25$ . At later  $t/T$ , lift normalized by instantaneous dynamic pressure declines monotonically, especially for the experimental cases, which fall below the quasi-steady value (that is, below 1) at  $t/T \sim 0.6$ . Approaching  $t/T = 0.75$ , there is a rise in lift. Overall, departure from quasi-steady response becomes greater with increasing  $\lambda$ . The lift-values from Isaacs' theory appear artificially large in this presentation, because the Isaacs' values are normalized by the static viscous lift coefficient (an experimentally measured force coefficient, not dynamic pressure). Were Isaacs' formulation normalized by  $2\pi\alpha$ , it too would be 1 at  $t/T = 0$ .

## Conclusions

A blade section in streamwise oscillation was taken to be a model of a retreating helicopter rotor blade section including reversed flow conditions. The lift histories for different amplitudes of streamwise oscillations, reduced frequency, and advance ratio were measured experimentally and computed numerically for a NACA0012 at both low and high incidence. Numerical and experimental flow visualization was performed to identify key flow features and provide physical insight into the lift histories.

For a blade section at low incidence, lift histories for all of the measured cases show similar trends. During the first quarter of the semi-stroke, lift increases and reaches a maximum near  $t/T = 0.25$ , when the dynamic pressure is maximum, in accordance with Isaacs' theoretical model. At this incidence, the flow is largely attached during the entire advancing stroke and only shows signs of separation when the relative velocity is lowest.

For a blade section at high incidence, lift histories become strongly dependent on advance ratio and reduced frequency. The peak lift generally increases with  $\lambda$  and  $k$ , and a phase lead arises with respect to the motion, likely as a result of viscous interactions. Flow is fully separated throughout most of the cycle. Isaacs' inviscid model strongly overpredicts peak lift and is unable to predict the phase lead. There is a fair agreement between the computational and experimental peak lift for moderate advance ratios and reduced frequencies, but computations do not predict the phase lead observed in experiments.

## References

- <sup>1</sup>Carter Jr, J., "High Speed Rotor Aircraft," US Patent 6,435,453, 2002.
- <sup>2</sup>Blackwell, R. and Millott, T., "Dynamics Design Characteristics of the Sikorsky X2 Technology Demonstrator Aircraft," Annual Forum Proceedings (AHS), Vol. 64, 2008.
- <sup>3</sup>Johnson, W., Yamauchi, G. K., and Watts, M. E., "NASA Heavy Lift Rotorcraft Systems Investigation," NASA TP 213467, 2005.
- <sup>4</sup>Harris, F. D., "Rotor Performance at High Advance Ratio," NASA CR 215370, 2008.
- <sup>5</sup>Ormiston, R., "Rotor Aerodynamic Characteristics at High Advance Ratio Relevant to Compound Rotorcraft," AHS Future Vertical Lift Aircraft Design Conference Proceedings, Jan. 2012.
- <sup>6</sup>Quakenbush, T. and Wachspress, D., "Measurement and Analysis of High Advance Ratio Rotor Performance," Proc. of the 64th AHS Forum, 2008.
- <sup>7</sup>Quakenbush, T., Wachspress, D., McKillip, R. M. J., and Sibilia, M. J., "Experimental and Analytical Studies of Lifting Rotor Performance at High Advance Ratios," Proc. of the AHS Aeromechanics Specialists Conference, January, 2010.
- <sup>8</sup>Berry, B. and Chopra, I., "Slowed Rotor Wind Tunnel Testing of an Instrumented Rotor at High Advance Ratio," Proc. of the 40th ERF, September 2014.
- <sup>9</sup>Bowen-Davies, G. and Chopra, I., "Validation of Rotor Performance and Loads at High Advance Ratio," 5th Decennial AHS Aeromechanics Specialists Conference Proceedings, January 2014.
- <sup>10</sup>Norman, T. R., Shinoda, P., Peterson, R. L., and Datta, A., "Full-Scale Wind Tunnel Test of the UH-60A Airloads Rotor," Proc. of the AHS 67th Forum, 2011.
- <sup>11</sup>Datta, A., Yeo, H., and Norman, T. R., "Experimental Investigation and Fundamental Understanding of a Slowed UH-60A Rotor at High Advance Ratios," Proc. of the AHS 67th Forum, May, 2011.
- <sup>12</sup>Montaudouin, J., Heo, S., Smith, M., and Bauchau, O., "Aerodynamic and Aeroelastic Analysis of Rotors at High Advance Ratio," Proc. of the 36th ERF, 2010.
- <sup>13</sup>Bowen-Davies, G. and Chopra, I., "Performance and Loads Correlation of the UH-60 Rotor at High Advance Ratios," Proc. of the 40th ERF, Sept. 2014.
- <sup>14</sup>Hodara, J. and Smith, M. J., "Improvement of Crossflow Aerodynamic Predictions for Forward Flight at All Advance Ratios," Proc. of the 40th ERF, September 2014.
- <sup>15</sup>Hodara, J., Lind, A. H., Jones, A. R., and Smith, M. J., "Collaborative Investigation of the Aerodynamic Behavior of Airfoils in Reverse Flow," Proc. of the 71st AHS Forum, May 2015.
- <sup>16</sup>Smith, M. J., Liggett, N. D., and Koukol, B. C., "Aerodynamics of Airfoils at High and Reverse Angles of Attack," *Journal of Aircraft*, Vol. 48, (6), 2011, pp. 2012–2023.
- <sup>17</sup>Lind, A. H., Smith, R. S., Milluzzo, J. I., and Jones, A. R., "Reynolds Number Effects on Airfoils in Reverse Flow (AIAA paper 15-1973)," 53rd AIAA Aerospace Sciences Meeting, Jan. 2015.
- <sup>18</sup>Greenberg, J. M., "Airfoil in Sinusoidal Motion in a Pulsating Stream," NACA TN 1326, 1947.
- <sup>19</sup>Isaacs, R., "Airfoil Theory for Rotary Wing Aircraft," *Journal of the Aeronautical Sciences*, Vol. 13, (4), 1946.
- <sup>20</sup>Leishman, J. G., *Principles of Helicopter Aerodynamics*, Cambridge University Press, New York, NY, 2000, Chapter 10.
- <sup>21</sup>Harris, F., *Introduction to Autogyros, Helicopters, and Other V/STOL Aircraft, Volume 1: Overview and Autogyros*, NASA/SP-2011-215959 Vol I, Moffatt Field, CA, 2011.
- <sup>22</sup>Granlund, K., Monnier, B., Ol, M., and Williams, D., "Airfoil longitudinal gust response in separated vs. attached flows," *Physics of Fluids*, Vol. 26, 2014. doi: 10.1063/1.4864338



<sup>23</sup>Smith, M. J., Koukol, B., Quackenbush, T., and Wachspress, D., “Reverse- and Cross-Flow Aerodynamics for High Advance-Ratio Flight,” 2009.

<sup>24</sup>Ol, M. V., Bernal, L., Kang, C.-K., and Shyy, W., “Shallow and deep dynamic stall for flapping low Reynolds number airfoils,” *Experiments in Fluids*, Vol. 46, (5), April 2009, pp. 883–901.  
doi: 10.1007/s00348-009-0660-3

<sup>25</sup>Darracq, D., Champagneux, S., and Corjon, A., “Computation of Unsteady Turbulent Airfoil Flows with an Aeroelastic AUSM+ Implicit Solver (Paper AIAA 1998-2411),” 16th AIAA Applied Aerodynamics Conference, June 1998.

<sup>26</sup>Sanchez-Rocha, M., Kirtas, M., and Menon, S., “Zonal Hybrid RANS-LES Method for Static and Oscillating Airfoils and Wings (AIAA paper 06-1256),” 44th AIAA Aerospace Sciences Meeting & Exhibit, Jan. 2006.

<sup>27</sup>Liggett, N. and Smith, M. J., “Temporal Convergence Criteria for Time-Accurate Viscous Simulations of Separated Flows,” *Computers & Fluids*, Vol. 66, doi: 10.1016/j.compfluid.2012.06.010, 2012, pp. 140–156.

<sup>28</sup>Spalart, P. R., “Young-Person’s Guide to Detached-Eddy Simulation Grids,” Technical report, NASA CR-2001-211032, 2001.

<sup>29</sup>Le Pape, A., Richez, F., and Deck, S., “Zonal Detached Eddy Simulation (ZDES) of an airfoil in post-stall condition (AIAA paper 12-3287),” 42nd AIAA Fluid Dynamics Conference and Exhibit, June 2012.

<sup>30</sup>Strelets, M., “Detached Eddy Simulation of Massively Separated Flows (AIAA paper 01-0879),” 39th AIAA Aerospace Sciences Meeting & Exhibit, Jan. 2001.

<sup>31</sup>Bunge, U., Mockett, C., and Thiele, F., “Guidelines for Implementing Detached-Eddy Simulation Using Different Models,” *Aerospace Science and Technology*, Vol. 11, (5), 2007, pp. 376–385.

Georgia Tech Contact:  
Prof. Marilyn Smith, marilyn.smith@ae.gatech.edu

Univ. of Maryland Contact:  
Prof. Anya Jones, arjones@umd.edu

Air Force Research Lab Contact:  
Dr. Michael Ol, michael.ol@us.af.mil